https://doi.org/10.1038/s41591-022-01749-8

nature medicine

OPEN

Check for updates

Stratification of radiosensitive brain metastases based on an actionable S100A9/RAGE resistance mechanism

Cátia Monteiro[1,41], Lauritz Miarka[1,41], María Perea-García[1], Neibla Priego[1], Pedro García-Gómez[1], Laura Álvaro-Espinosa[1], Ana de Pablos-Aragoneses[1], Natalia Yebra[1], Diana Retana[1], Patricia Baena[1], Coral Fustero-Torre[2], Osvaldo Graña-Castro[2], Kevin Troulé[2], Eduardo Caleiras[3], Patricia Tezanos[4], Pablo Muela[4], Elisa Cintado[4], José Luis Trejo[4], Juan Manuel Sepúlveda[5], Pedro González-León[6], Luis Jiménez-Roldán[6,7], Luis Miguel Moreno[6], Olga Esteban[6], Ángel Pérez-Núñez[6,7], Aurelio Hernández-Lain[8], José Mazarico Gallego[9], Irene Ferrer[10,11], Rocío Suárez[10,11], Eva M. Garrido-Martín[10,11], Luis Paz-Ares[9,10,11,12], Celine Dalmasso[13], Elizabeth Cohen-Jonathan Moyal[13], Aurore Siegfried[14], Aisling Hegarty[15], Stephen Keelan[15], Damir Varešlija[15], Leonie S. Young[15], Malte Mohme[16], Yvonne Goy[17], Harriet Wikman[18], Jose Fernández-Alén[19], Guillermo Blasco[19], Lucía Alcázar[19], Clara Cabañuz[20], Sergei I. Grivennikov[21,39], Andrada Ianus[22], Noam Shemesh[22], Claudia C. Faria[23,24], Rebecca Lee[25,26], Paul Lorigan[25,26], Emilie Le Rhun[27], Michael Weller[27], Riccardo Soffietti[28], Luca Bertero[29], Umberto Ricardi[30], Joaquim Bosch-Barrera[31,32,33], Elia Sais[31,32], Eduard Teixidor[31,32], Alejandro Hernández-Martínez[31,32], Alfonso Calvo[11,34], Javier Aristu[35], Santiago M. Martin[36], Alvaro Gonzalez[37], Omer Adler[38], Neta Erez[38], RENACER* and Manuel Valiente[1]✉

Whole-brain radiotherapy (WBRT) is the treatment backbone for many patients with brain metastasis; however, its efficacy in preventing disease progression and the associated toxicity have questioned the clinical impact of this approach and emphasized the need for alternative treatments. Given the limited therapeutic options available for these patients and the poor understanding of the molecular mechanisms underlying the resistance of metastatic lesions to WBRT, we sought to uncover actionable targets and biomarkers that could help to refine patient selection. Through an unbiased analysis of experimental in vivo models of brain metastasis resistant to WBRT, we identified activation of the S100A9–RAGE–NF-κB–JunB pathway in brain metastases as a potential mediator of resistance in this organ. Targeting this pathway genetically or pharmacologically was sufficient to revert the WBRT resistance and increase therapeutic benefits in vivo at lower doses of radiation. In patients with primary melanoma, lung or breast adenocarcinoma developing brain metastasis, endogenous S100A9 levels in brain lesions correlated with clinical response to WBRT and underscored the potential of S100A9 levels in the blood as a noninvasive biomarker. Collectively, we provide a molecular framework to personalize WBRT and improve its efficacy through combination with a radiosensitizer that balances therapeutic benefit and toxicity.

The brain is a common metastatic location, and 20–40% of patients with solid tumors eventually develop lesions in the central nervous system, mostly spreading from lung and breast cancer or melanoma[1]. The development of effective therapeutic agents has remained a challenge, and most patients succumb to the disease less than 12 months after diagnosis[2–4]. Upon diagnosis, current clinical management of brain metastasis frequently includes radiotherapy, owing to its superior ability to access the brain and treat both local and distant intracranial lesions[5].

Historically, whole-brain radiation therapy (WBRT) was the gold standard in the management of patients with brain metastasis. Although WBRT may control symptoms and decrease the incidence of intracranial failure as well as local recurrences, clinical trials did not demonstrate an effect on overall survival (OS) or quality of life when compared with supportive care[6–9]. Adding to this controversial role of WBRT, patients receiving radiotherapy usually show a high incidence of neurocognitive decline due to irradiation of healthy brain tissue[10–12]. Owing to the concerns associated with WBRT, clinical practice adopted stereotactic radiosurgery (SRS), a strategy to deliver a high dose of radiation specifically to metastatic lesions, as new standard of care for numerous indications in the management of brain metastasis[10,12,13]. However, WBRT continues to be an important treatment option. Patients may present with multifocal disease with lesions that are too large in size for SRS[14–16]. In addition, the use of SRS is associated with a higher incidence of radionecrosis than WBRT[17–19]. Thus, the limited efficacy of WBRT and the frequent recurrence of metastatic lesions within the irradiated field suggest the emergence of a profound resistance to irradiation.

A full list of affiliations appears at the end of the paper.

Limited research has been devoted to the study of radiotherapy in preclinical brain metastasis models. In a triple-negative breast cancer (TNBC) and a lung cancer brain metastasis model a single dose of irradiation delivered to established metastases confirmed the clinically observed resistance to WBRT[20,21]. However, these and other studies[22,23] do not faithfully recapitulate the clinical scenario, in which WBRT is not delivered in a single dose of radiation but as a hypofractionated protocol[7]. Previous works reported increased survival in mice with brain metastasis treated with a fractionated chemoradiotherapy protocol, but the phenotype was not reproduced with radiotherapy only[24]. A similar finding was made in established brain lesions with an experimental model of breast cancer brain metastasis using clinically adapted WBRT protocol of 3 Gy per day for 10 days[25]. None of these studies provided any molecular explanation for the emergence of radioresistance.

To address this clinically relevant problem, we characterized the resistance to radiation using mouse models, brain metastasis organotypic cultures established from patients who are radioresistant and several clinically annotated cohorts of patients with melanoma, lung or breast cancer with brain metastasis.

Here, we report that brain metastatic cancer cells from different primary tumors are induced to highly express S100A9 within the brain microenvironment, which mediates resistance to radiotherapy by downstream activation of NF-κB. Genetic or pharmacological targeting of S100A9 by the blood–brain barrier–permeable inhibitor FPS-ZM1 of its receptor, RAGE (receptor for advanced glycation end products), potently sensitizes brain metastasis to irradiation in experimental models of brain metastasis as well as in patient-derived organotypic cultures. Furthermore, S100A9 expression in human brain metastasis from patients with lung cancer, breast cancer or melanoma correlates with benefit from radiotherapy. Taken together, our findings suggest the use of S100A9 as a clinically relevant biomarker to personalize radiotherapy for patients with brain metastasis and the inhibitor FPS-ZM1 as a radiosensitizing agent.

Results

Experimental brain metastases do not respond to WBRT. Three different protocols of hypofractionated WBRT[24–26] were applied to established brain metastases after intracardiac (IC) inoculation of the lung adenocarcinoma cell line H2030-BrM (ref. [27]) (Extended Data Fig. 1a and Fig. 1a). None of them halted the progression of the disease (Fig. 1b), and mice died at the same time as nonirradiated controls (Extended Data Fig. 1b). Histological analysis of irradiated brain metastasis confirmed maintenance of the proliferative rate in contrast to the significant decrease observed when radiation was applied to extracranial tumors (Supplementary Fig. 1a–c). To confirm this finding, we irradiated established E0771-BrM brain metastases, a organotropic syngeneic model (Supplementary Fig. 1e and f) derived from a TNBC cell line[28]. In this case, we had to perform intracranial injection of the cancer cells providing sufficient time to complete the WBRT schedule (Supplementary Fig. 1g). This is necessary because IC injection of E0771-BrM leads to very extensive extracranial disease (Supplementary Fig. 1h) that develops faster than intracranial metastasis. Similarly, irradiation was not effective to control the progression of E0771-BrM in the brain (Supplementary Fig. 1i,j) in contrast to extracranial metastases (Supplementary Fig. 1k,l). Given the radioresistance of brain metastasis in vivo, we evaluated the response to irradiation in vitro. Irradiation of H2030-BrM, E0771-BrM and eight additional BrM cell lines in vitro (Fig. 1c and Supplementary Fig. 1d) reproduced the high radiosensitivity of BrM cells outside the brain.

Fig. 1 | Acquired radioresistance in experimental brain metastasis. a, Representative BLI of mice injected IC with H2030-BrM before and after completing different radiation schedules. The colored lines indicate the specific condition/irradiation protocol as specified in **b**. Color bars show BLI intensity in p s^{-1} cm^{-2} sr^{-1}). **b**, Quantification of BLI in the head of mice. Values correspond to the fold increase for each mouse before, week 2 after IC injection of H2030-BrM and after completing each radiation schedule week 4 after IC injection. Values are shown in box-and-whisker plots, where each dot is a mouse and the line in the box corresponds to the median. The boxes go from the upper to the lower quartiles, and the whiskers go from the minimum to the maximum value ($n=10$, mice nonirradiated; $n=9$, mice irradiated with 10 × 3 Gy; $n=9$, mice irradiated with 3 × 5.5 Gy; $n=10$, mice irradiated with 3 × 3 Gy). *P* value was calculated using two-tailed *t*-test between nonirradiated and irradiated experimental groups (nonirradiated versus 10 × 3 Gy, $P=0.7065$; nonirradiated versus 3 × 5.5 Gy, $P=0.7109$; nonirradiated versus 3 × 3 Gy, $P=0.9556$). γ-IR, gamma irradiation; NS, not significant. **c**, Representative images of the cell density (blue, bisbenzimide) 72 h after irradiating H2030-BrM cells compared with nonirradiated control. Heatmap showing the sensitivity of ten different brain tropic cancer cell lines to irradiation 72 h after a single dose of 10 Gy. Heatmap colors correspond to the percentage of cells remaining after irradiation normalized to the nonirradiated control. Values were obtained from three replicates per experimental condition (mean percentage of viable cells after irradiation ± s.e.m.; *P* value was calculated using a two-tailed *t*-test (1, H2030-BrM: 27.63 ± 1.25, $P=0.0046$; 2, 393N1: 48.77 ± 12.34, $P=0.0200$; 3, 482N1: 47.25 ± 2.57, $P=0.0154$; 4, PC9-BrM: 28.66 ± 6.81, $P=0.0013$; 5, MDA231-BrM: 14.12 ± 3.35, $P=0.0010$; 6, CN34-BrM: 47.46 ± 1.98, $P=0.0068$; 7, E0771-BrM: 27.63 ± 1.25, $P=0.0046$; 8, HCC1954-BrMa: 28.28 ± 3.87, $P=0.0023$; 9, HCC1954-BrMb: 29.78 ± 1.25, $P=0.0064$; 10, ErbB2-BrM: 34.38 ± 4.78, $P=0.0155$)). Colored bars: blue, lung cancer-derived brain tropic models (1, H2030-BrM and 4, PC9-BrM: human cell lines; 2, 393N1 and 3, 482N1: mouse cell lines); pink, breast cancer-derived brain tropic models (5, MDA231-BrM, 6, CN34-BrM, 8, HCC1954-BrMa and 9, HCC1954-BrMb: human cell lines; 7, E0771-BrM and 10, ErbB2-BrM: mouse cell lines); black, *KRAS/Kras* and *TRP53/Trp53* mutants; red, *EGFR* mutant; brown, TNBC; green, $HER2^+$ breast cancer. Scale bar, 5 µm. **d**, Representative images of brain organotypic cultures with metastatic cells 72 h after irradiation at 10 Gy. Color bar shows BLI intensity in p s^{-1} cm^{-2} sr^{-1}). **e**, Quantification of photon flux values from metastatic cells growing in organotypic brain cultures after irradiation normalized to preirradiated BLI values. Values are shown in box-and-whisker plots where every dot represents an independent culture and the line in the box corresponds to the median. The boxes go from the upper to the lower quartiles, and the whiskers go from the minimum to the maximum value ($n=23$, nonirradiated brain slices with H2030-BrM; $n=24$, irradiated brain slices with H2030-BrM). *P* value was calculated using a two-tailed *t*-test. **f**, Working model suggesting potential sources of radioresistance and how to model them in vitro. **g**, Representative images of oncospheres 72 h after irradiation at 10 Gy. Scale bar, 250 µm. **h**, Quantification of oncosphere area. Values are shown in box-and-whisker plots, where every dot represents a different well from which the mean area of all oncospheres were quantified, from an independent culture and the line in the box corresponds to the median. The boxes go from the upper to the lower quartiles, and the whiskers go from the minimum to the maximum value ($n=8$, nonirradiated wells with H2030-BrM oncospheres; $n=10$, irradiated wells with H2030-BrM oncospheres). *P* value was calculated using a two-tailed *t*-test. **i**, Representative images of co-cultures between H2030-BrM (GFP^+) and glial cells (astrocytes, $GFAP^+$) 72 h after irradiation (10 Gy). Scale bar, 250 µm. **j**, Quantification of GFP^+ BrM cells after radiation normalized to their respective nonirradiated controls from the experiment shown in **i**. Values are shown in box-and-whisker plots, where every dot represents an independent culture and the line in the box corresponds to the median. The boxes go from the upper to the lower quartiles, and the whiskers go from the minimum to the maximum value ($n=11$, H2030-BrM; $n=5$ H2030-BrM in indirect co-culture with glia cells; $n=5$, H2030-BrM in direct co-culture with glia cells; $n=6$, H2030-BrM in direct co-culture with astrocytes). *P* values were calculated using a two-tailed *t*-test.

A transcriptional signature correlates with radioresistance. We asked whether the mere contact with the brain tissue might unlock the activation of radioresistance mechanisms. H2030-BrM or E0771-BrM cells plated on live brain slices cultured ex vivo[29] (Extended Data Fig. 1c) and treated with the same irradiation protocol that reduced their viability under standard culture conditions in vitro (Fig. 1c) did not reproduce a therapeutic benefit (Fig. 1d,e and Extended Data Fig. 1d,e). BrM cells plated on brain slices adapt to this culture by interacting with the surrounding microenvironment[29,30] (Fig. 1f) that, by the reanalysis of published data[31], involved transcriptional changes compatible with the acquisition of stem cell-like properties (Extended Data Fig. 1f and Supplementary Table 1), which might be required to reinitiate the tumor at secondary organs[32,33]. Consequently, we hypothesized that in vitro protocols enriching tumor-initiating properties and co-culturing BrM cells with components of the microenvironment might also induce radioresistance (Fig. 1f).

Oncospheres, which are thought to have increased cancer stem cell properties and thus metastatic ability[34], from H2030-BrM and E0771-BrM cells treated with the same irradiation dose tested under standard culture conditions in vitro (Fig. 1c) showed radioresistance (Fig. 1g,h and Extended Data Fig. 1g,h).

The ability of metastatic cells to interact with glial cells seems to be critical to colonize the brain[35] and can involve both physical contact[36,37] and paracrine interactions[38,39]. Interestingly, co-culture between BrM cells and glial cells[40], particularly astrocytes, increased resistance to radiation only when the culture included direct heterotypic cell–cell contacts (Fig. 1i,j and Extended Data Fig. 1i,j).

Based on these findings, we performed RNA sequencing (RNA-seq) on all sensitive and resistant in vitro conditions 24 h after applying radiation, when cell viability was not compromised (Supplementary Fig. 2a,b). Although transcriptomic differences were evident between the two radioresistant culture conditions (oncospheres and co-cultures) (Supplementary Fig. 2c

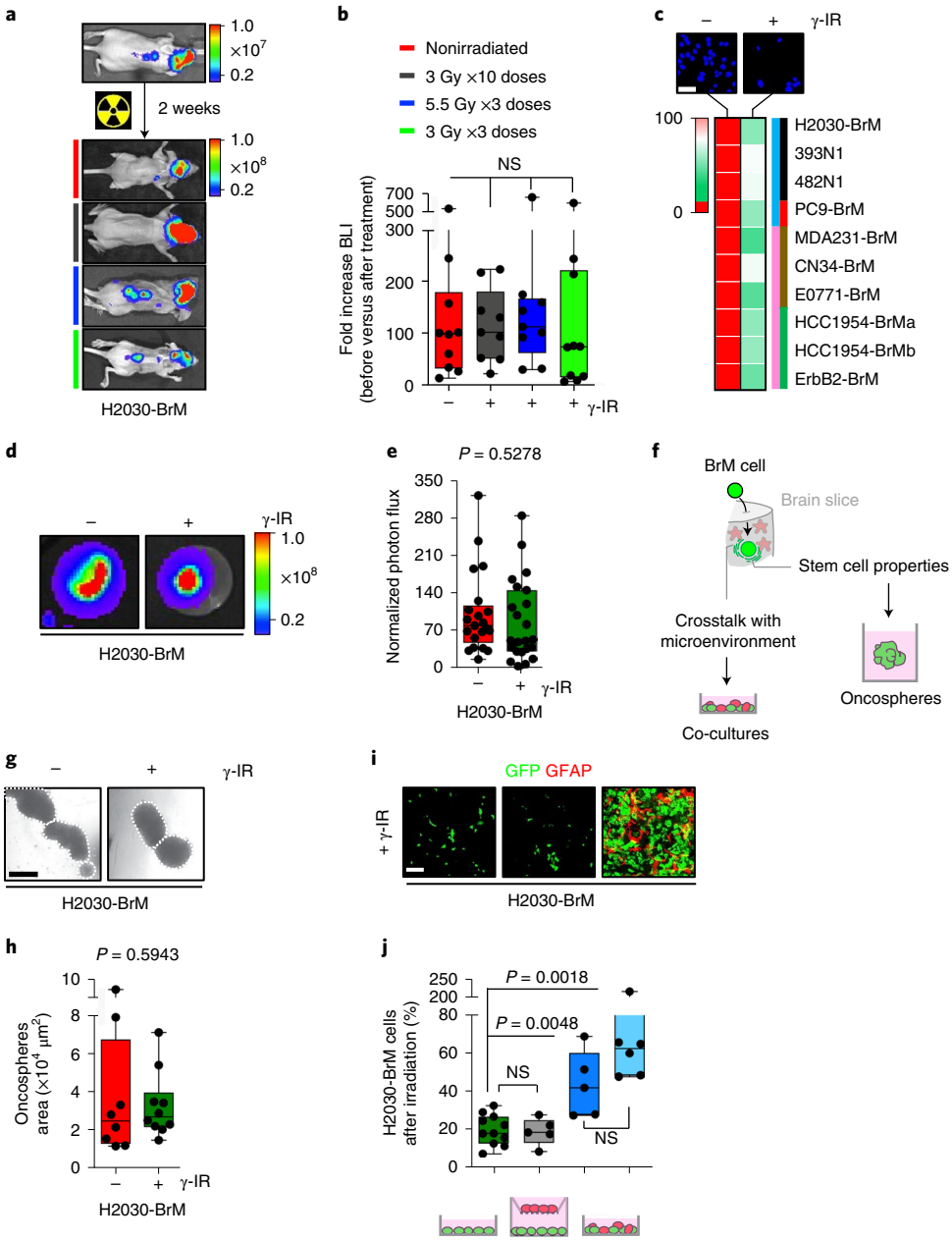

and Supplementary Table 2), we also identified a discrete commonly deregulated gene signature (Fig. 2a, Supplementary Fig. 2d,e and Supplementary Table 3). Interestingly, this signature was also present in cancer cells plated on brain organotypic cultures (Supplementary Table 4)[31], denoting *S100A9* as the top upregulated gene (Extended Data Fig. 2a and Supplementary Table 5). We further validated the induction of S100A9 in cancer cells ex vivo (Supplementary Fig. 2f,g) and in vivo in experimental (Fig. 2b) and human (Fig. 2c) brain metastases.

Thus, our data suggest that S100A9 expression is induced in cancer cells under specific contexts correlating with the acquisition of radioresistance.

Astrocyte-released cytokines induce S100A9 secretion in cancer cells. Our in vitro and ex vivo radioresistance paradigms might involve different mechanisms mediating the induction of S100A9 in cancer cells (that is, acquisition of stem cell properties versus the influence of the microenvironment) (Fig. 1f). When we explored changes of murine cytokines in the brain microenvironment affected by metastases, we identified CXCL1, CCL2 and CCL4 as the only ones that were significantly upregulated compared with the normal brain (Supplementary Fig. 2i). Among these, only CXCL1 secretion was also increased in astrocytes by direct co-culture with cancer cells (Supplementary Fig. 2j). Additionally, our previous research identified tumor-necrosis factor α (TNF-α), interferon-α and TGF-α as the top upregulated cytokines in astrocytes upon direct co-culture with brain metastatic cells[36]. Because interferon-α and TGF-α were not included in our unbiased approach (Supplementary Fig. 2i), we interrogated whether any of them induced *S100A9* expression in cancer cells and concluded that only TGF-α did so (Fig. 2e and Supplementary Fig. 2k). Similarly, recombinant CXCL1 was confirmed to induce *S100A9* expression in brain metastatic cells (Fig. 2d). Addition of each individual cytokine was sufficient to increase the radioresistance of H2030-BrM cells in vitro (Extended Data Fig. 2b,e). Finally, we validated the presence of CXCL1 and TGF-α in metastasis-associated astrocytes (Extended Data Fig. 2c,f) and the corresponding receptors, CXCR2 and EGFR, respectively, in metastatic cells in situ (Extended Data Fig. 2d,g). Overall, our data suggest that the induction of S100A9 in brain metastasis might be the consequence of an inflammatory response initiated by the direct contact between reactive astrocytes and cancer cells (Fig. 2j).

S100A9 is frequently secreted into the extracellular space and binds to Toll-like receptor 4 or RAGE[41]. We first hypothesized that the presence of S100A9 in the extracellular space might be involved in the acquisition of radioresistance because the protein generated by cancer cells could only be detected in the conditioned media (CM) of organotypic brain cultures, but not in the one obtained from adherent cultures in vitro of the same BrM cell line (Fig. 2f). In addition, when recombinant S100A9 was added to radiosensitive BrM cells growing under adherent conditions in vitro, a threefold induction of resistance to radiotherapy was detected (Fig. 2g). The transcriptomic profile of radioresistant preparations suggested that RAGE activity was induced upon radiation (Extended Data Fig. 2h,i), which we validated in situ in experimental (Fig. 2h) and human brain metastases (Extended Data Fig. 2j). Binding of S100A9 to RAGE has been shown to activate numerous signaling cascades, including NF-κB[42,43]. Although this signaling pathway was previously reported to be involved in radioresistance of glioblastoma and other contexts[44–46], it has not been linked to S100A9 or therapeutic resistance in brain metastasis. Remarkably, the transcriptomic profile of radioresistant preparations showed enriched NF-κB signaling pathways (Supplementary Fig. 2h and Supplementary Table 6) that was confirmed in metastatic cells receiving irradiation in brain organotypic cultures (Fig. 2i).

Thus, our data suggest that metastatic cells in the brain induce the expression and secretion of S100A9, which, through radiation-induced RAGE receptor expression, might activate NF-κB-mediated radioresistance (Fig. 2j). We subsequently decided to functionally validate this working model.

Targeting S100A9 radiosensitizes experimental brain metastases. Cancer-related phenotypes ascribed to S100A9 include its

Fig. 2 | Contact-dependent astrocyte-released cytokines induce S100A9 secretion in cancer cells, triggering NF-κB activation. a, Heatmap representing color-coded expression levels of commonly deregulated genes in H2030-BrM cell line when cultured under radiosensitive (purple line, adherent; light green line, co-culture with inserts) compared with radioresistant (dark green line, oncospheres; blue line, cell–cell co-culture) conditions in vitro. Only genes with false discovery rate (FDR) < 0.05 and a $\log_2$ ratio >1 were considered. **b**, Representative images of S100A9 protein expression levels in metastatic lesions growing in brains from mice IC injected with H2030-BrM and E0771-BrM. Three brains were analyzed in each BrM model. Scale bars, 120 μm (H2030-BrM) and 50 μm (E0771-BrM). **c**, Sixty-six human brain metastases from patients with lung cancer (33 cases) or breast cancer (30 cases) or other primary tumors (3 cases) were stained for S100A9 by immunohistochemistry. Representative images are shown. Scale bar, 50 μm. Quantification of different histological scoring of cancer cells is shown in pie charts. Five cases had to be excluded; 27 of 61 were scored with no staining (score 0), 9 of 61 with weak staining (score 1), 12 of 61 with moderate staining (score 2) and 13 of 61 with strong staining (score 3). **d**, Quantification of *S100A9* expression levels in H2030-BrM after stimulation with 100 ng ml^{-1} recombinant CXCL1 (rCXCL1) or control. Values are shown in dot plots, and dots represent independent experiments. The line in the box corresponds to the median. The boxes go from the upper to the lower quartiles, and the whiskers go from the minimum to the maximum value ($n = 7$, each experimental condition). *P* value was calculated Wilcoxon signed rank test, two sided. **e**, Quantification of *S100A9* expression levels in H2030-BrM after stimulation with recombinant transforming growth factor α (rTGF-α) or control. Values are shown in dot plots and dots represent independent experiments. The line in the box corresponds to the median. The boxes go from the upper to the lower quartiles, and the whiskers go from the minimum to the maximum value ($n = 7$, each experimental condition). *P* value was calculated using two-tailed *t*-test. **f**, Quantification by enzyme-linked immunosorbent assay (ELISA) of human S100A9 (hS100A9) in the supernatant of H2030-BrM grown either under adherent conditions in vitro or in organotypic cultures ex vivo. Values are shown in box-and-whisker plots, where every dot represents an independent experiment and the line in the box corresponds to the median. The boxes go from the upper to the lower quartiles, and the whiskers go from the minimum to the maximum value ($n = 6$, H2030-BrM adherent cultures; $n = 8$, H2030-BrM growing in organotypic brain cultures). *P* value was calculated using two-tailed Mann–Whitney test. **g**, Quantification of in vitro viable cell fraction after irradiation at 10 Gy and 200 ng ml^{-1} recombinant hS100A9 or control, as determined by manual cell counting of bisbenzimide-positive nuclei. Values are percentages of viable cells respect to unirradiated controls and shown in a dot plot, where each dot represents an independent experiment and the line in the box corresponds to the median ($n = 3$, each experimental condition). *P* value was calculated using a two-tailed *t*-test. **h**, Representative pictures of RAGE immunohistochemistry from unirradiated or irradiated established H2030-BrM metastases in vivo. Scale bar, 50 μm. **i**, Quantification of the percentage of NF-κB$^+$ GFP$^+$ H2030-BrM cells identified by the expression of an engineered mCherry NF-κB activity reporter. Brain slices with cancer cells were evaluated 72 h after treatment with radiotherapy. Values are shown in box-and-whisker plots where each dot is a brain organotypic culture ($n = 11$, nonirradiated; $n = 7$, irradiated with a single dose of 10 Gy) and the line in the box corresponds to the median. The boxes go from the upper to the lower quartiles and the whiskers go from the minimum to the maximum value. *P* value was calculated using a two-tailed *t*-test. **j**, Schema of working model of radioresistance in brain metastasis.

involvement as an inducer of invasion[47,48] that has been linked to the premetastatic niche[49,50] as well as to chemoresistance driven by the recruitment of myeloid cells to lung metastases[51] or in a cell-autonomous manner[52]. Knockdown of *S100A9* in H2030-BrM cells (Supplementary Fig. 3a) did not impair the growth rate of metastatic cells ex vivo in organotypic cultures (Supplementary Fig. 3b–d) or in vivo in brain metastasis (Supplementary Fig. 3e,f). Remarkably, *S100A9* genetic loss of function sensitized brain metastasis to radiation in organotypic culture conditions (Supplementary Fig. 3b–d). Encouraged by these results, we performed an in vivo experiment applying a protocol of WBRT mimicking the clinical approach (Fig. 1b) to our preclinical model once lung cancer brain metastasis with downregulated *S100A9* levels were established (Fig. 3a)[53]. This genetic loss of function reverted the acquired resistance of H2030-BrM brain metastases to radiotherapy in vivo (Fig. 3b,c), even to half dose of radiation (Fig. 3c). At the end of the experiment, histological analyses confirmed a major reduction in the number of metastases with barely detectable levels of S100A9 (Extended Data Fig. 3a,b). Given the notable reduction in brain metastasis burden, we wondered whether the genetic strategy could even provide a survival benefit in spite of the concomitant progressive disease extracranially (Fig. 3b). Remarkably, both knockdown targeting *S100A9* in H2030-BrM cancer cells were sufficient to extend OS when combined with radiotherapy (Fig. 3d).

Given that our previous data suggested that S100A9-dependent radioresistance could also apply to other experimental BrM models independently of primary origin (Extended Data Fig. 1d,e,g–j), we evaluated the role of S100A9 in E0771-BrM, a TNBC brain

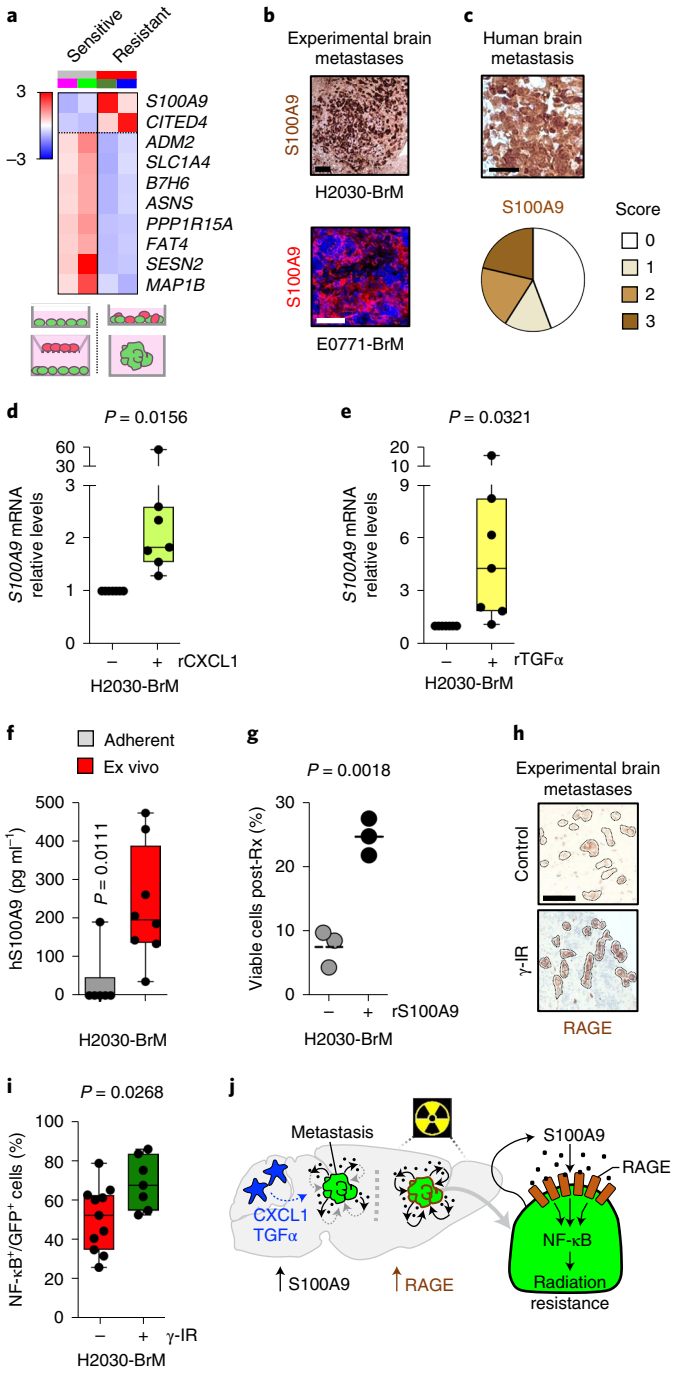

metastasis syngeneic model (Supplementary Fig. 1e–h) resistant to WBRT (Supplementary Fig. 1i,j). Similar to the lung adenocarcinoma model, *s100a9* loss of function (Supplementary Fig. 3g) did not generate any phenotype in vivo before treatment (Supplementary Fig. 3h,i). However, when the WBRT protocol was applied to established E0771-BrM intracranial tumors with reduced S100A9 levels (Extended Data Fig. 3c), a significant reduction of brain metastases was observed (Extended Data Fig. 3d,e).

In order to determine whether S100A9 was the main contributor to NF-κB activity under radioresistant conditions (Fig. 2i and Supplementary Fig. 2h), we evaluated a pathway-dependent fluorescent reporter for NF-κB activity (mCherry$^+$)[54,55] in the context of S100A9 loss of function (Extended Data Fig. 3f) in H2030-BrM cells expressing constitutively GFP. The increased percentage of double fluorescent mCherry$^+$/GFP$^+$ cancer cells after irradiation ex vivo was abrogated when S100A9 was targeted (Fig. 3e). Similarly, analysis of cancer cells with activated NF-κB signaling (mCherry$^+$/ GFP$^+$) after irradiation in vivo confirmed their dependency on S100A9 (Extended Data Fig. 3g). Furthermore, we identified nine NF-κB targets upregulated under radioresistant conditions (Extended Data Fig. 3h and Supplementary Table 12). Out of these, we confirmed S100A9-dependent JunB induction upon irradiation (Fig. 3f) and presence in human brain metastasis (Extended Data Fig. 3i,j).

S100A9 has also been reported in neutrophils and monocytes besides cancer cells[42,43]. Indeed, we detected S100A9 in a small fraction (8.3%) of the brain metastasis microenvironment (Fig. 3g,h), mainly represented by neutrophils but with measurable contributions from Iba1$^+$ and GFAP$^+$ cells, namely microglia/macrophages and reactive astrocytes, respectively (Fig. 3g and Extended Data Fig. 3k). Given that our previous loss-of-function approach (Fig. 3a, Extended Data Fig. 3c) did not consider the noncancer compartment and that S100A9$^+$ cells in the microenvironment are represented by multiple cell types (Fig. 3g), we generated a genetically engineered mouse model with the *S100a9* gene knocked out (Supplementary Fig. 3m) to evaluate its potential contribution to the resistance phenotype. Interestingly, the E0771-BrM cell line, which colonized the brain of knockout mice indistinguishably from control mice (Supplementary Fig. 3j,k), remained resistant to WBRT when the microenvironment expressed no S100A9 (Fig. 3i–k and Extended Data Fig. 3l,m). Complementary, the significant reduction in brain metastases upon *S100A9* knockdown in cancer cells did not correlate with changes in the number of infiltrating neutrophils (Supplementary Fig. 3l). Thus, cancer-derived S100A9 in brain metastasis appears to be necessary and sufficient for radioresistance in experimental lung and breast cancer models.

S100A9-mediated radioresistance is actionable and linked to cancer stem cell properties. Although local aggressiveness of metastatic cells could increase their exposure to the microenvironment, we found S100A9 in an indolent metastasis model[56] (Supplementary Fig. 4a) and, complementary, variably expressed at the invasive front of human brain metastases (Supplementary Fig. 4b). Thus, we explored the identity of S100A9$^+$ cells in situ using single-cell RNA-seq (scRNA-seq)[57] (Extended Data Fig. 4a).

Metastatic cells were allocated into nine clusters (Extended Data Fig. 4b and Supplementary Table 7), with six of them showing detectable expression levels of *S100A9* (Extended Data Fig. 4c), in agreement with a more abundant expression in cancer cells than in

Fig. 3 | Targeting S100A9 in cancer cells radiosensitizes experimental lung and breast cancer brain metastases in a NF-κB–JunB-dependent manner. **a**, Schema of experimental design. **b**, Representative BLI of mice 5 weeks after being inoculated IC with H2030-BrM control (left), sh*S100A9*#1 (middle) or sh*S100A9*#2 (right) cells and treated with 10 × 3 Gy irradiation using the WBRT protocol depicted in **a**. Ex vivo brain BLI is also shown for each condition. Color bars show BLI intensity in p s^{-1} cm^{-2} sr^{-1}. BLI colour bars correspond to in vivo (top) and ex vivo (bottom). **c**, Quantification of in vivo photon flux values from the head of mice inoculated with H2030-BrM control, sh*S100A9*#1 or sh*S100A9*#2 cells that received WBRT, as depicted in **a**. BLI was performed at three different time points during the course of treatment (weeks 1, 3 and 5). Values are shown in box-and-whisker plots, where every dot represents a different brain and the line in the box corresponds to the median. The boxes go from the upper to the lower quartiles, and the whiskers go from the minimum to the maximum value ($n = 9$, H2030-BrM control; $n = 8$, H2030-BrM sh*S100A9*#1; $n = 8$, H2030-BrM sh*S100A9*#2). *P* value was calculated using two-tailed *t*-test. **d**, Kaplan–Meier plot showing survival proportions of mice inoculated with H2030-BrM control, sh*S100A9*#1 or sh*S100A9*#2 cells that received WBRT as depicted in **a** ($n = 12$, each experimental condition). *P* value was calculated using a log-rank (Mantel–Cox) test. OS, overall survival. **e**, Quantification of the percentage of NF-κB$^+$ GFP$^+$ positive H2030-BrM control, sh*S100A9*#1 or sh*S100A9*#2 cells in organotypic cultures, which received no or 10 Gy irradiation. Values are shown in box-and-whisker plots, where every dot represents an independent culture and the line in the box corresponds to the median. The boxes go from the upper to the lower quartiles and the whiskers go from the minimum to the maximum value ($n = 13$, H2030-BrM control; $n = 13$, H2030-BrM control + γ-IR; $n = 6$, sh*S100A9*#1 + γ-IR; $n = 9$, sh*S100A9*#2 + γ-IR). *P* values were calculated using two-tailed *t*-tests. Upper panel shows representative organotypic cultures from the experiment in the panel. Scale bar, 75 µm. **f**, Quantification of the percentage of JunB$^+$ GFP$^+$ BrM cells in nonirradiated H2030-BrM control and irradiated H2030-BrM control, H2030-BrM sh*S100A9*#1 or H2030-BrM sh*S100A9*#2 brain metastatic lesions. Values are shown in box-and-whisker plots, where every dot represents a metastatic lesion and the line in the box corresponds to the median. The boxes go from the upper to the lower quartiles, and the whiskers go from the minimum to the maximum value ($n = 10$ metastases from 2 animals, H2030-BrM control; $n = 15$ metastases from 2 animals, H2030-BrM control + γ-IR; $n = 16$ metastases from 3 animals, H2030-BrM sh*S100A9*#1 + γ-IR; $n = 19$ metastases from 3 animals, H2030-BrM sh*S100A9*#2 + γ-IR). *P* values were calculated using two-tailed Mann–Whitney tests. Upper panel shows representative organotypic cultures from the experiment in the panel. Scale bar, 75 µm. **g**, Representative images of an established H2030-BrM brain metastasis and its microenvironment. The S100A9 antibody used for this staining is rodent specific to stain only the microenvironment and not human cancer cells. Arrowheads point to S100A9$^+$ cells in the microenvironment. CC, cancer cells. The image is representative of the five independent brains evaluated. Scale bars, 50 µm (left panel) and 10 µm (right panels). **h**, Quantification of S100A9$^+$ BB$^+$ cells in the microenvironment of brain metastasis. Only GFP$^-$ cells were quantified to exclude cancer cells. Pie chart represents S100A9$^+$ GFP$^-$ BB$^+$ cells as the red slice (8.29%) and S100A9$^-$ GFP$^-$ BB$^+$ cells as the white slice. Cells were quantified in nine fields of view (FOVs) representing equally different sizes of metastasis from three mice brains. **i**, Schema of experimental design. **j**, Representative bioluminescence and immunofluorescent images of ex vivo brains from S100A9$^{+/+}$ or S100A9$^{-/-}$ mice 2 weeks after intracranial injection of E0771-BrM cells. After inoculation, mice were consequently treated with WBRT as shown in **i**. Neutrophils are labeled with NIMP-R14 antibody (green). The bioluminescence images are representative of the 15 brains analyzed, and the immunofluorescence images are representative of the six brains analyzed. Color bar shows BLI intensity in p s^{-1} cm^{-2} sr^{-1}). Scale bar, 25 µm. **k**, Quantification of ex vivo brain photon flux values from S100A9$^{+/+}$ or S100A9$^{-/-}$ mice inoculated with E0771-BrM cells and treated with WBRT as depicted in **i**. Values are shown in box-and-whisker plots, where every dot represents a different brain and the line in the box corresponds to the median. The boxes go from the upper to the lower quartiles, and the whiskers go from the minimum to the maximum value ($n = 10$, S100A9$^{+/+}$ mice; $n = 16$, S100A9$^{-/-}$ mice). *P* value was calculated using Mann–Whitney test, two sided. KO, knockout; WT, wild-type.

the microenvironment (Fig. 3h). However, *S100A9*, together with *S100A8*, were the two genes with the most variable expression pattern among cancer cells (Supplementary Fig. 4d and Supplementary Table 8). Indeed, we validated the established[43] functional dependency between them (Supplementary Fig. 4e,f). Interestingly, the highest values of *S100A9* expression correspond to cluster 5 (Fig. 4a and Supplementary Table 9), which was enriched in stem cell signatures among other features previously linked to radioresistance, such as epithelial-mesenchymal transition, glycolytic metabolism and DNA repair[58] (Fig. 4b, Extended Data Fig. 4d and Supplementary Table 10). Hence, to test whether S100A9$^+$ cells have cancer stem cell properties, we evaluated their ability to form oncospheres[34]. We first identified a cell surface marker from S100A9$^+$ cancer cells. CD55 was selected as part of the overlap between differentially expressed genes in patients with high levels of *S100A9*, scored in a published cohort of breast cancer brain metastases[59], and the in vitro and ex vivo radioresistant surrogates (Fig. 4c, Supplementary Fig. 2d and Supplementary Table 11). After confirming the correlation of CD55 and S100A9 in H2030-BrM brain metastases (Fig. 4d), sorted CD55$^+$ and CD55$^-$ cancer cells (Supplementary Fig. 4c) were subjected to oncosphere assays. Only the CD55$^+$ fraction of cancer cells formed oncospheres (Fig. 4e,f), contained S100A9$^+$ cells (Fig. 4e) independently of the culture condition (Supplementary Fig. 4g) and recapitulated the gene expression signature of cluster 5 (Fig. 4g and Supplementary Table 9).

In spite of the high therapeutic resistance presumably linked to S100A9 (Fig. 4b and Supplementary Table 10), we tested pharmacological inhibitors against various pathway components (Fig. 4h). We treated organotypic cultures containing brain metastatic cells with inhibitors targeting RAGE (FPS-ZM1) or NF-κB (BAY117082) in combination with radiotherapy (Fig. 4h). The results obtained demonstrate the ability of both inhibitors to revert acquired radioresistance (Fig. 4i,j and Supplementary Fig. 4h,i).

S100A9 is a brain metastasis biomarker of therapeutic response to WBRT. Given the correlation between S100A9 and radioresistance in brain metastasis models and the presence of the pathway in human samples (Fig. 2c, Extended Data Fig. 2j, Extended Data Fig. 3i and Supplementary Table 13), we explored a potential correlation with radioresistance in patients. First, we confirmed the presence of S100A9$^+$ cancer cells independently of the primary source of the metastasis (Fig. 5b and Supplementary Table 14); of note, the percentage was lower in melanoma brain metastases than in lung or breast cancer (Fig. 5b). Interestingly, in contrast to experimental models of brain metastasis derived from lung cancer or breast cancer (Fig. 2b, Supplementary Fig. 2f,g, Extended Data Figs. 3a and 4d and

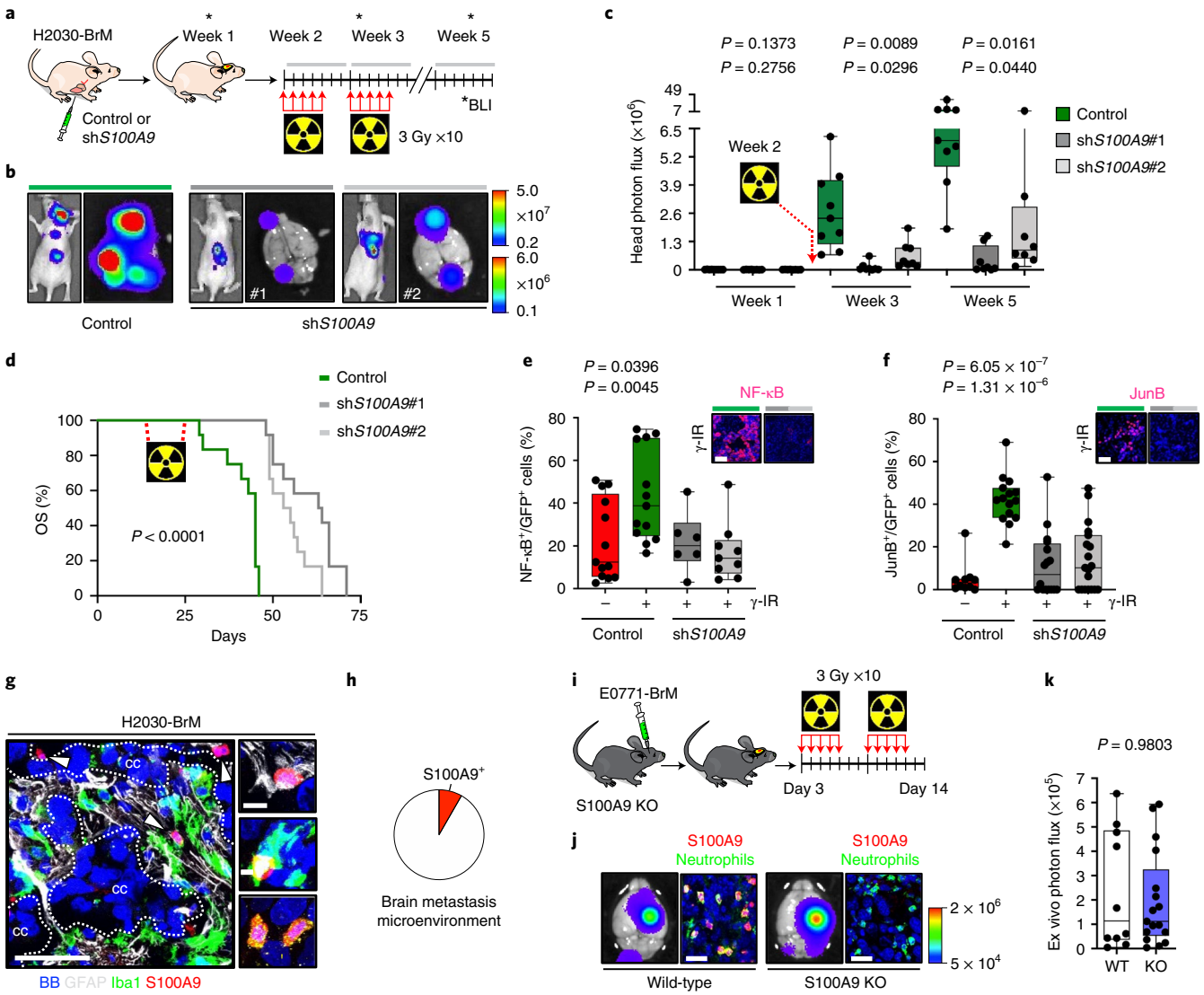

Supplementary Fig. 4a), we were unable to find a melanoma brain metastasis model expressing S100A9 (Supplementary Fig. 5a), potentially suggesting that a specific subtype of melanoma brain metastases, not represented by available mouse models, could be the main contributor to S100A9 positivity. To score the clinical correlation with S100A9, several cohorts of patients with brain metastasis and lung cancer ($n=22$), breast cancer[59,60] ($n=42$) or melanoma ($n=34$) were selected based on the presence of patients who received neurosurgery followed by radiotherapy (Fig. 5a and Supplementary Tables 15–17). S100A9 levels in lung cancer brain metastases obtained by neurosurgery correlated with the time for brain relapse after WBRT, as measured by follow-up magnetic resonance imaging (MRI) (Fig. 5c,d and Supplementary Table 15). However, patients treated with SRS, a different modality of radiotherapy involving high-dose radiation targeted to small and highly localized areas, could not be correlated with S100A9 levels, because no relapses were detected (Supplementary Fig. 5b and Supplementary Table 18). Analysis of the cohort of patients with breast cancer brain metastases[59,60] who were treated with radiotherapy confirmed the correlation between *S100A9* expression levels and survival from brain metastasis diagnosis (Fig. 5e and Supplementary Table 16), which was reproduced by *S100A8* (Supplementary Fig. 5c,d and Supplementary Table 16), as in experimental models (Supplementary Fig 4e,f). Of note, the clinical correlation was independent of *S100A9* levels in the primary tumor[59] (Supplementary Fig. 5e,f). An additional cohort including patients with brain metastases from breast cancer and melanoma reproduced the clinical correlation between S100A9 and radiation response (Fig. 5f and Supplementary Table 17).

Furthermore, a similar correlation of *S100A9* with shorter survival was also detected in two independent cohorts of glioblastoma (Supplementary Fig. 5g,h and Supplementary Table 19), a primary brain tumor including focal brain radiotherapy as part of the standard of care[61]. In contrast, The Cancer Genome Atlas (TCGA) data including irradiated primary tumors from lung (Supplementary Fig. 5i) or breast cancer (Supplementary Fig. 5j) did not show a correlation between progression-free survival and *S100A9* levels (Supplementary Table 20).

Thus, S100A9 should be considered as a biomarker to predict therapeutic response of brain metastases to WBRT. In addition, our findings indicate that the same resistance mechanism might be extended to primary brain tumors, but not necessarily to extracranial ones.

Only a subpopulation of patients with secondary brain tumors are candidates for neurosurgery given the limitations imposed by the number and location of metastases as well as the presence of extracranial systemic disease and associated overall status of the patient[16]. Consequently, to expand the biomarker strategy to patients not eligible for neurosurgery and given the secretory nature of S100A9 (Fig. 2f), we tested the clinical correlation between S100A9 and response to radiotherapy in noninvasive liquid biopsy specimens. A total of 71 patients with brain metastases from any cancer type who received WBRT and had available blood samples as liquid biopsy specimens were analyzed (Fig. 5g and Supplementary Table 21). Strikingly, circulating S100A9 levels before or immediately after receiving WBRT correlated with survival from the diagnosis of brain metastasis (Fig. 5h and Supplementary Table 21). Of note, S100A9 levels in the blood did not show any clinical correlation with survival in those patients with brain metastases that did not receive WBRT (Supplementary Fig. 5k and Supplementary Table 21). No other variable such as age or Karnofsky Performance Status score correlate with S100A9 (Supplementary Fig 5l,m and Supplementary Tables 15–17, 21 and 22). However, to be conclusive about these additional variables, a larger prospective clinical study is required.

FPS-ZM1 radiosensitizes experimental and human brain metastases. To explore the possibility of providing an additional therapeutic option for those patients with high levels of S100A9 rather than just neglect the use of WBRT, we took advantage of our ex vivo results showing that the RAGE inhibitor FPS-ZM1 radiosensitized brain metastasis (Fig. 4i and Supplementary Fig 4h). Given

Fig. 4 | S100A9-mediated radioresistance is linked to cancer stem cell properties and sensitivity to RAGE and NF-κB inhibition. a, Uniform manifold approximation and projection (UMAP) plot of all analyzed cancer cells showing *S100A9* gene expression. Color corresponds to the gene expression in each cell. Dotted line surrounds cluster 5. **b**, GSEA of genes deregulated in cluster 5 versus all other clusters, corresponding to Supplementary Table 10. Displayed gene sets are the 25 highest ranking up- or downregulated gene sets according to the normalized enrichment score (NES) and a cutoff of *P* value < 0.05 and FDR < 0.25. Colored bars correspond to the biological category these gene sets belong to. EMT, epithelial–mesenchymal transition. ATR, ataxia aelangiectasia and Rad3-related protein. **c**, Venn diagram showing the strategy delineating CD55 by intersecting genes upregulated in S100A9^{high} patients with genes upregulated in in vitro and ex vivo radioresistant culture conditions (Supplementary Table 11). **d**, Representative flow cytometry dot plot illustrating the double staining CD55/S100A9 in permeabilized cancer cells sorted from H2030-BrM brain metastases. Q, quartile. **e**, Left: representative BLI images of oncospheres generated from CD55$^-$ and CD55$^+$ sorted cells from H2030-BrM brain metastases. Representative brightfield images of respective oncospheres are also shown in the smaller panels. Arrowheads point to oncospheres. Scale bar, 125 µm. Right: representative immunofluorescent image of S100A9 staining in CD55$^+$ oncospheres. Color bar shows BLI intensity in p s^{-1} cm^{-2} sr^{-1}). Scale bar, 25 µm. **f**, Quantification of numbers of oncospheres per well from CD55$^-$ and CD55$^+$ sorted cells. Values are shown in box-and-whisker plots, where every dot represents an individual well from three independent experiments and the line in the box corresponds to the median. The boxes go from the upper to the lower quartiles, and the whiskers go from the minimum to the maximum value ($n=30$ wells, each experimental condition). *P* value was calculated using a two-tailed *t*-test. **g**, Heatmap displaying gene expression values of 11 genes, selected from highly upregulated genes of cluster 5 of the single-cell analysis in **a**, in CD55$^+$ and CD55$^-$ oncospheres. Color-coded values depicted are fold-changes normalized to CD55$^-$ oncospheres (fold increase, CD55$^+$/CD55$^-$: *S100A9*, 36.91; *TGM2*, 50.96; *TOP2A*, 10.01; *SPP*, 7.52; *ANGPTL4*, 0.82; *RSPO3*, 4.63; *STC1*, 1.32; *IGFBP3*, 167.68; *FAM83A*, 148.97; *ACOX2*, 34.60; *CITED4*, 4.19). **h**, Schema illustrating pharmacological approaches to evaluate the working model of radioresistance. **i**, Representative images and quantification of photon flux values from H2030-BrM cells growing in organotypic brain cultures treated with 10 µM of FPS-ZM1 after irradiation. Values at endpoint (day 3) were first normalized to values from the same culture before treatment (day 0). Values are shown in box-and-whisker plots, where every dot represents an independent culture and the line in the box corresponds to the median. The boxes go from the upper to the lower quartiles, and the whiskers go from the minimum to the maximum value ($n=13$, nonirradiated H2030-BrM; $n=12$, irradiated H2030-BrM, both treated with FPS-ZM1). *P* value was calculated using a two-tailed *t*-test. **j**, Representative images and quantification of brain organotypic cultures with H2030-BrM cells 72 h after treatment with 50 µM BAY-117081, an inhibitor of IκB-α phosphorylation, and 10 Gy irradiation or no irradiation. Quantification of photon flux values at endpoint (day 3) were normalized to values from the same culture before treatment (day 0). Values are shown in box-and-whisker plots, where every dot represents an independent culture and the line in the box corresponds to the median. The boxes go from the upper to the lower quartiles, and the whiskers go from the minimum to the maximum value ($n=12$, nonirradiated H2030-BrM; $n=12$, irradiated H2030-BrM, both treated with BAY-117081). *P* value was calculated using a two-tailed *t*-test. Color bar in **i** and **j** shows BLI intensity in p s^{-1} cm^{-2} sr^{-1}).

the extraordinary ability of FPS-ZM1 to cross the blood–brain barrier[62], we tested it in combination with WBRT. Once lung adenocarcinoma brain metastases were established, we provided WBRT together with the RAGE inhibitor (Fig. 6a). Both bioluminescence imaging (BLI) (Fig. 6b,c) and histology (Supplementary Fig. 6a–c) confirmed the ability of FPS-ZM1 to potentiate the benefits of radiation without evidence of increased toxicity (Supplementary Fig. 6d) while effectively decreasing the levels of the radioresistance pathway component JunB (Supplementary Fig. 6e,f). As reported with the genetic approach (Supplementary Fig. 3l), the reduction in brain metastasis with the combination therapy did not decrease the presence of neutrophils (Supplementary Fig. 6g). As a validation to further considering FPS-ZM1 as a radiosensitizer for brain metastases independently of the primary origin, we confirmed the therapeutic benefit over radiation alone in the TNBC model E0771-BrM (Extended Data Fig. 5a–c and Supplementary Fig. 6h,i).

To extend the proof-of-concept to human metastases, we applied the combination therapy ex vivo to brain metastases that relapsed after surgery and WBRT (Fig. 6d and Supplementary Table 22). Relapsed metastases obtained by a second neurosurgery were evaluated for S100A9 levels and processed to generate patient-derived organotypic cultures (PDOCs), which is an ideal platform for testing combination therapies, as we previously reported[53]. In addition to relapsed samples, we included a newly diagnosed, S100A9-negative brain metastasis with no previous local treatment (Extended Data Fig. 5d and Supplementary Table 22), which was sensitive

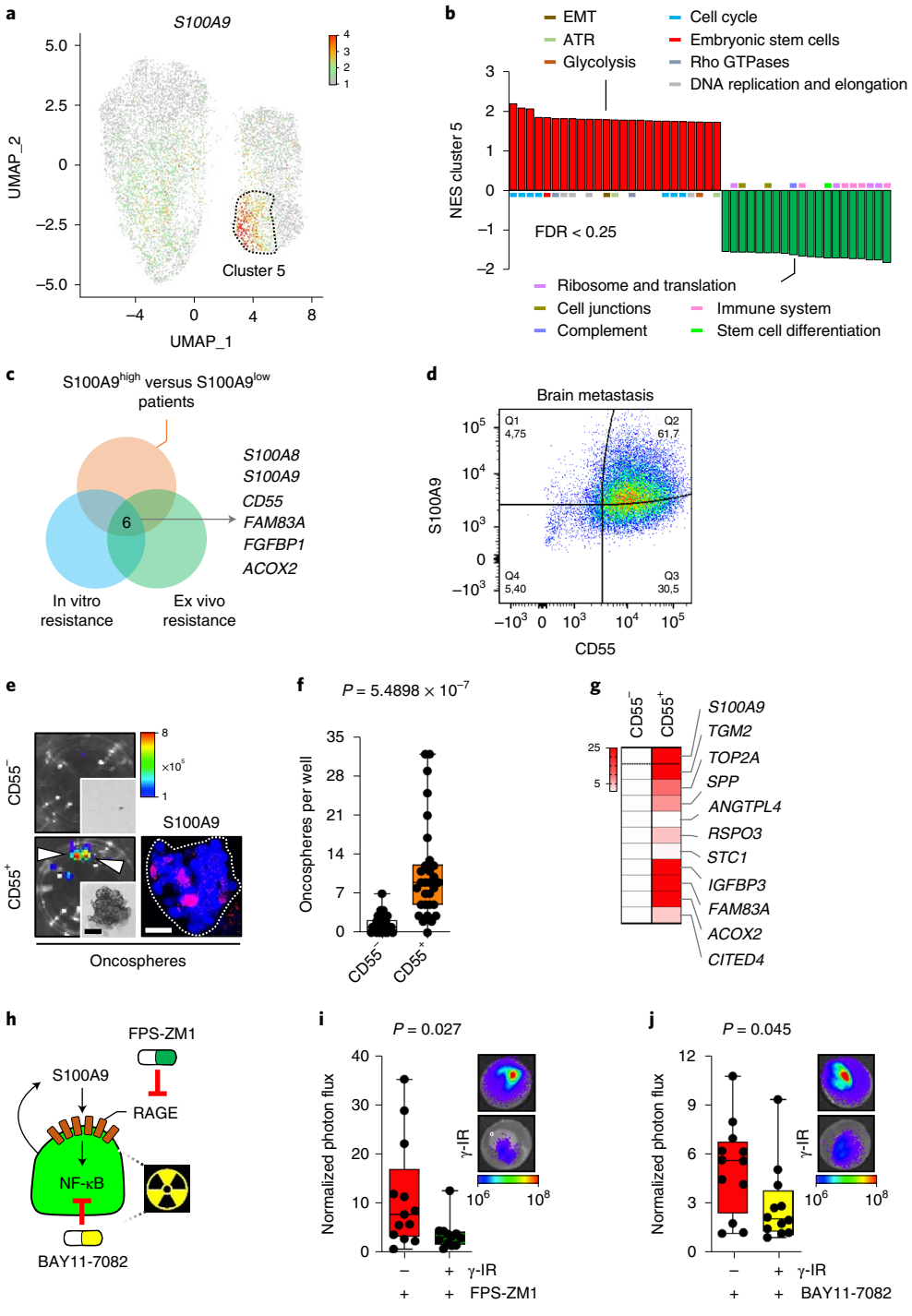

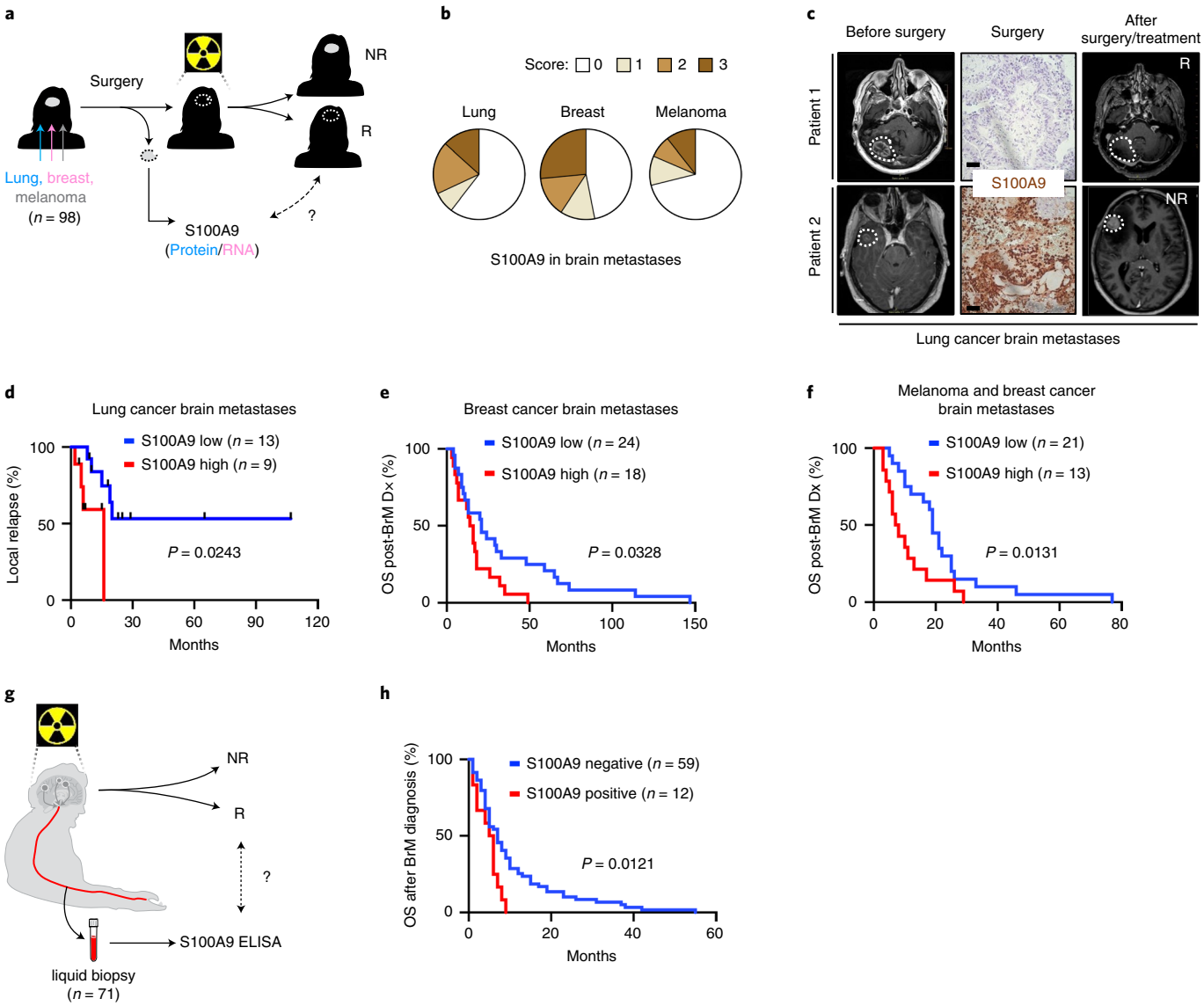

Fig. 5 | S100A9 is a brain metastasis biomarker of therapeutic response to WBRT. a, Schema of study design. S100A9 protein or mRNA levels, respectively, were assessed in 22 patients with lung cancer brain metastases, 62 patients with breast cancer brain metastases and 14 patients with melanoma brain metastases who underwent neurosurgery and were subsequently treated with radiotherapy. S100A9 was correlated with response to radiotherapy. R, responder; NR, nonresponder. **b**, A total of 140 human brain metastases from patients with lung cancer (53 cases), breast cancer (49 cases) or melanoma (38 cases) were stained for S100A9 by immunohistochemistry. Quantification of different histological scoring of cancer cells is shown in pie charts separate for each primary tumor. For lung cancer, 32 of 53 were scored with no staining (score 0), 4 of 53 with weak staining (score 1), 10 of 53 with moderate staining (score 2) and 7 of 53 with strong staining (score 3). For breast cancer, 23 of 49 were scored with no staining, 6 of 49 with weak staining, 7 of 49 with moderate staining and 13 of 49 with strong staining. For melanoma, 27 of 38 were scored with no staining, 4 of 38 with weak staining, 3 of 38 with moderate staining and 4 of 38 with strong staining. **c**, Representative MRI images of two lung cancer brain metastasis patients before and after neurosurgery and WBRT. For each patient the corresponding S100A9 immunohistochemical staining is shown. The images shown are representative of the 22 patients analyzed. Scale bar, 100 µm. **d**, Analysis of time to local relapse, as evaluated by follow-up MRI, after neurosurgery and WBRT in a cohort of 22 patients with lung cancer brain metastases. Data are shown as a Kaplan–Meier plot, and two groups of patients (S100A9 low/high) were delineated by using 5% of S100A9 immunohistochemical staining positivity as a cutoff. *P* value was calculated using a log-rank (Mantel–Cox) test. **e**, Analysis of survival after brain metastasis diagnosis in a cohort of 42 patients with breast cancer brain metastases. Only patients who received adjuvant radiotherapy were included. Data are shown as a Kaplan–Meier plot, and two groups of patients (S100A9 low/high) were delineated according to their *S100A9* mRNA expression levels in brain metastasis. *P* value was calculated using a log-rank (Mantel–Cox) test. **f**, Analysis of survival after brain metastasis diagnosis in a cohort of 34 patients with brain metastasis from breast cancer (20 cases) and melanoma (14 cases). Data are shown as a Kaplan–Meier plot, and two groups of patients (S100A9 low/high) were delineated by using 5% of S100A9 immunohistochemical staining positivity as a cutoff. *P* value was calculated using a log-rank (Mantel–Cox) test. **g**, Schema of study design. S100A9 protein was measured in liquid biopsy specimens from 71 patients with brain metastases who received WBRT. S100A9 positivity in serum was correlated with response to radiotherapy. **h**, Analysis of survival after brain metastasis diagnosis in a cohort of 71 patients with brain metastases from lung cancer (43 cases), breast cancer (14 cases), melanoma (10 cases) or other primary tumors (4 cases). Data are shown as a Kaplan–Meier plot, and two groups of patients (positive/negative) were delineated according to their S100A9 positivity in serum samples, collected before or within 2.5 months of receiving WBRT. *P* value was calculated using log-rank (Mantel–Cox) test. BrM, brain metastasis.

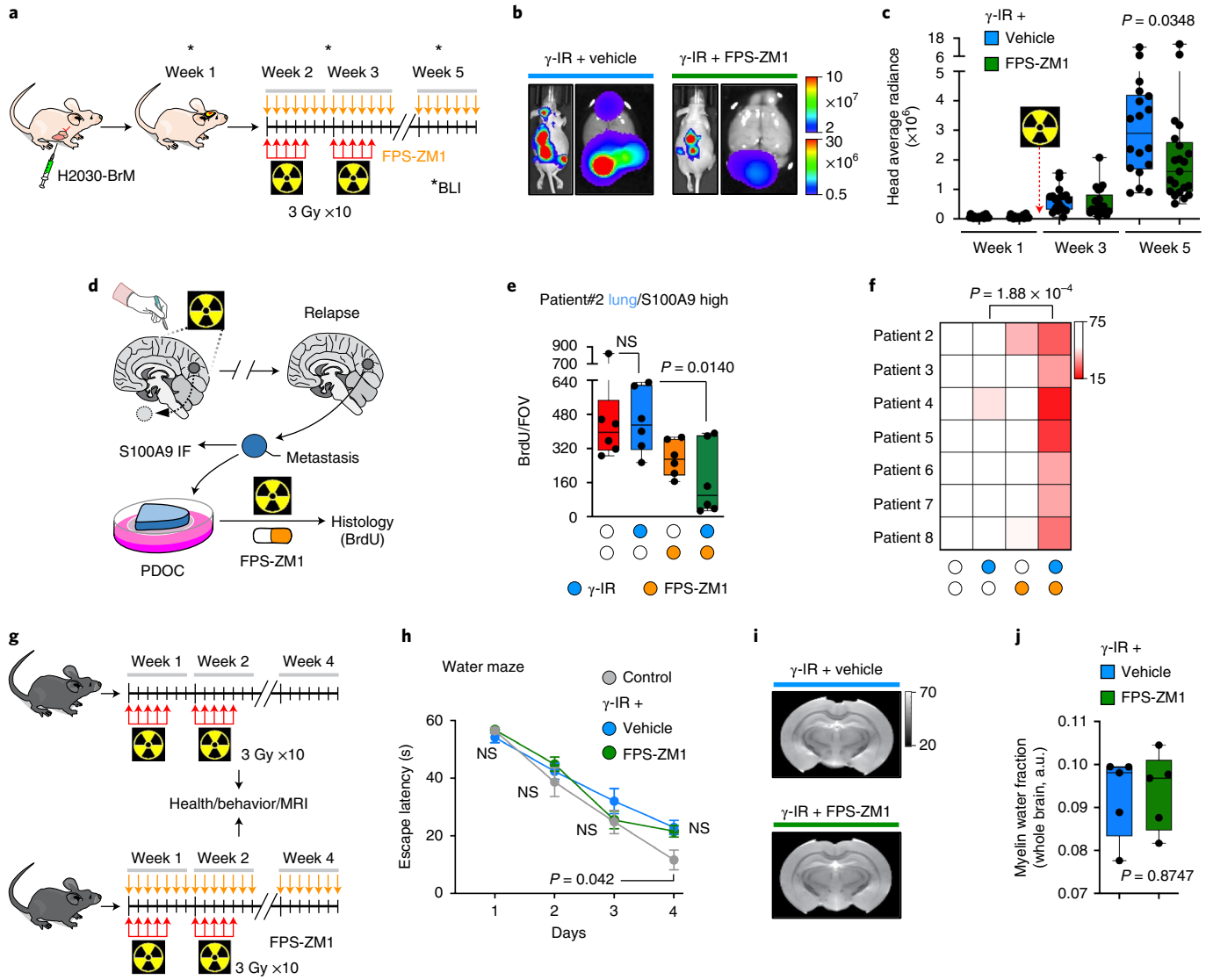

Fig. 6 | FPS-ZM1 radiosensitizes experimental and human brain metastases. a, Schema of experimental design. H2030-BrM cells were inoculated IC into nude mice, and 2 weeks later, mice received 10 doses of 3 Gy WBRT plus 500 mg kg^{-1} per day FPS-ZM1 or vehicle until the end of the experiment. Intracranial tumor growth was monitored weekly with BLI. **b**, Representative bioluminescence images in vivo and ex vivo (brains) of control and experimental arms at endpoint, 5 weeks after IC injection. BLI scale bars correspond to in vivo (top) and ex vivo (bottom). Colors bar show BLI intensity in p s^{-1} cm^{-2} sr^{-1}). **c**, Quantification of in vivo photon flux values from the head of mice inoculated with H2030-BrM cells that received WBRT plus vehicle or FPS-ZM1, as depicted in **a**. BLI was performed at three different time points during the course of treatment (weeks 1, 3 and 5). Values are shown in box-and-whisker plots, where every dot represents a different brain and the line in the box corresponds to the median. The boxes go from the upper to the lower quartiles, and the whiskers go from the minimum to the maximum value (n = 18, vehicle + γ-IR; n = 21, FPS-ZM1 + γ-IR). P value was calculated using two-tailed Mann–Whitney test. **d**, Schema of experimental design. Surgically resected human brain metastases from patients who relapsed after receiving previous local treatments, including WBRT, were used to measure S100A9 levels by immunofluorescence (IF) and establish PDOCs, which were treated with FPS-ZM1 (10 μM) with or without irradiation and the therapeutic benefit evaluated 3 days later by 5-bromodeoxyuridine (BrdU) incorporation in cancer cells. **e**, Quantification of BrdU$^+$ cancer cells in PDOCs from patient 2 treated with FPS-ZM1 and/or irradiation. Values are shown in box-and-whisker plots, where every dot represents an independent culture and the line in the box corresponds to the median. The boxes go from the upper to the lower quartiles, and the whiskers go from the minimum to the maximum value (n = 6, DMSO; n = 6, FPS-ZM1, n = 6, γ-IR; n = 6, FPS-ZM1 + γ-IR). P values were calculated using a two-tailed t-test. **f**, Heatmap depicting the quantification of BrdU$^+$ cancer cells in PDOCs derived from seven patients with relapsed brain metastases, which have S100A9 high levels. Each row represents an individual patient, and each column represents different treatment conditions. Color-coded values are percentages of BrdU$^+$ cancer cells normalized to the DMSO condition of each patient. P value was calculated using a two-tailed t-test. **g**, Schema of experimental design. Tumor-naive C57BL/6 mice received 10 doses of 3 Gy WBRT plus 500 mg kg^{-1} per day FPS-ZM1 or vehicle for 3 weeks. One month later, mice underwent health assessment, imaging and behavioral testing. **h**, Quantification of the time spent to escape the water to the platform (escape latency) from different groups of mice. Values are shown in a temporal scale, where each dot represents the mean value for each group in a given day of the test and the error bars represent s.e.m. (n = 6, control; n = 13, vehicle + γ-IR, n = 20, FPS-ZM1 + γ-IR). Calculation of P values is detailed in Supplementary Table 24. **i**, Representative ex vivo ultrahigh-field MRI images of brains from mice treated with either WBRT + vehicle or WBRT + FPS-ZM1 are shown. Greyscale shows the values from the long T2 component by ex vivo ultrahigh-field MRI. **j**, Quantification of whole-brain myelin water fraction by ex vivo ultrahigh-field MRI in brains from experiment depicted in **i**. Values are shown in box-and-whisker plots, where every dot represents a brain and the line in the box corresponds to the median. The boxes go from the upper to the lower quartiles, and the whiskers go from the minimum to the maximum value (n = 5, each experimental condition). P value was calculated using a two-tailed t-test.

to irradiation alone (Extended Data Fig. 5e) with no additional effects when radiation was combined with FPS-ZM1 (Extended Data Fig. 5e and Supplementary Table 22). In contrast, all relapsed metastases ($n=7$) showed high S100A9 levels (Extended Data Fig. 5d, Supplementary Fig. 6j–o and Supplementary Table 22), and, although resistant to radiation alone, when irradiation was combined with FPS-ZM1, all PDOCs were sensitized (Fig. 6e,f, Supplementary Fig. 6j–o and Supplementary Table 22).

In summary, we report a comprehensive strategy that not only identifies patients who could benefit from WBRT but also provide a combination therapy to overcome radioresistance.

Radiosensitizers have the main risk of affecting noncancer cells, which generates toxicity[63]. Therefore, we performed a comprehensive evaluation of both general and organ-specific aspects to conclude whether FPS-ZM1 acts as a nonspecific radiosensitizer in the brain. Two cohorts of mice were treated with the same radiotherapy schedule as the one applied to experimental metastases (Fig. 1b, Fig. 6g). The impact of radiotherapy in the normal brain is not immediate as established by previous publications[64]. Consequently, 1 month after finishing the treatment with radiation and FPS-ZM1, as a reference time point established by previous literature[65,66], mice were evaluated for their health status[67], trained in behavioral tests[68] measuring motor and neurocognitive functions (including anxiety/stress, learning and memory) and their brains scanned by ultrahigh-field MRI to evaluate subtle anatomical changes[69,70]. The health status (Supplementary Table 23), rotarod test (Supplementary Fig. 6p), elevated plus maze test (Extended Data Fig. 5f), water maze test (Fig. 6h), contextual fear conditioning test (Extended Data Fig. 5g), novel object recognition (NOR) test (Supplementary Fig. 6q) and pattern separation test (Supplementary Fig. 6r) results were indistinguishable between groups (Supplementary Table 24). Of note, the fourth day of the water maze test (Fig. 6h and Supplementary Table 24) might reflect a potential impact of irradiation on the ability to use hippocampal-dependent spatial maps, which would be an expected consequence of this therapy on neural stem cells[64]. Interestingly, FPS-ZM1 did not potentiate this deleterious consequence of irradiation (Fig. 6h and Supplementary Table 24). MRI analysis detected no specific anatomical differences between groups (Fig. 6i). A quantitative estimation of the brains' long T2 component and myelin water fraction also reached the same conclusion (Fig. 6j and Extended Data Fig. 5h).

Thus, because FPS-ZM1 did not generate any undesired neurotoxic effect when combined with radiotherapy in mice, its radiosensitizing effect does not seem to affect the healthy brain tissue and its function.

Discussion

In this report, we identify S100A9 as a common mediator of radioresistance in brain metastasis that is induced in cancer cells by interaction with the brain microenvironment. When irradiated, membranous expression of RAGE increases in metastatic cells, rendering them susceptible to S100A9-mediated resistance to WBRT. Strikingly, targeting the S100A9–RAGE axis pharmacologically with the blood–brain barrier-permeable RAGE inhibitor FPS-ZM1 restores sensitivity to radiotherapy in experimental models of brain metastasis in vivo as well as in patient-derived organotypic cultures. Because S100A9 expression correlates with poor response to radiotherapy, our findings present a novel approach to personalize radiotherapy. Based on S100A9 expression on surgical specimens or circulating levels detected by liquid biopsy, patients who would benefit from radiotherapy could be selected while patients with high resistance could be spared, thereby avoiding neurocognitive decline. Furthermore, the use of RAGE inhibitors could be used to lower the radiation dose necessary for killing tumor cells, thereby minimizing effects of irradiation on normal brain tissue and increasing the survival benefit in these patients.

In support of the highly translational nature of our findings, azeliragon or TTP488, a RAGE antagonist, has been under active investigation in clinical trials for Alzheimer's disease[71–73]. Here, it has been shown to be clinically safe at effective doses[71,73] and could therefore easily be repurposed to investigate its potential as a radiosensitizing agent in brain metastatic disease. Bearing the investigated effect of RAGE inhibition on Alzheimer's disease in mind, it has been demonstrated that RAGE is also expressed on neurons and glial cells[74,75]. Hence, our comprehensive analysis discards that RAGE inhibitors sensitize healthy brain tissue to ionizing radiation in agreement with the increased neuroprotection described in RAGE knockout mice when affected by ischemic brain damage[76,77].

Our results, together with recent data[52], suggest that the acquisition of therapeutic resistance in brain metastasis might be linked to the induction of cellular plasticity mechanisms activated by the crosstalk with the microenvironment during colonization. The interface between the microenvironmental influence on cell plasticity and the pre-existing heterogeneity within cancer cells might promote the emergence of specific cellular and functional phenotypes (that is, cancer stem cells) that could be therapeutically relevant. Such context-specific mechanisms of cancer cell plasticity could inspire novel strategies aiming to expand personalized cancer care beyond those targeting the genomic alterations of the tumor, thus contributing to increase the limited therapeutic options available for the majority of patients with tumors in the central nervous system.

Although further studies are warranted to dissect the S100A9-dependent molecular mechanisms promoting radioresistance, a multicentric prospective study and subsequent clinical trial within the National Network of Brain Metastasis (RENACER) will further evaluate our strategy to personalize the use of radiotherapy.

Online content

Any methods, additional references, Nature Research reporting summaries, source data, extended data, supplementary information, acknowledgements, peer review information; details of author contributions and competing interests; and statements of data and code availability are available at https://doi.org/10.1038/s41591-022-01749-8.

Received: 14 May 2021; Accepted: 16 February 2022;
Published online: 11 April 2022

References

1. Cagney, D. N. et al. Incidence and prognosis of patients with brain metastases at diagnosis of systemic malignancy: a population-based study. *Neuro. Oncol.* **19**, 1511–1521 (2017).
2. Berghoff, A. S. et al. Descriptive statistical analysis of a real life cohort of 2419 patients with brain metastases of solid cancers. *ESMO Open* **1**, e000024 (2016).
3. Valiente, M. et al. The evolving landscape of brain metastasis. *Trends Cancer* **4**, 176–196 (2018).
4. Eichler, A. F. et al. The biology of brain metastases-translation to new therapies. *Nat. Rev. Clin. Oncol.* **8**, 344–356 (2011).
5. Le Rhun, E. et al. EANO-ESMO Clinical Practice Guidelines for diagnosis, treatment and follow-up of patients with brain metastasis from solid tumours. *Ann. Oncol.* **32**, 1332–1347 (2021).
6. Mulvenna, P. et al. Dexamethasone and supportive care with or without whole brain radiotherapy in treating patients with non-small cell lung cancer with brain metastases unsuitable for resection or stereotactic radiotherapy (QUARTZ): results from a phase 3, non-inferiority, randomised trial. *Lancet* **388**, 2004–2014 (2016).
7. Tsao, M. N. et al. Whole brain radiotherapy for the treatment of newly diagnosed multiple brain metastases. *Cochrane Database Syst. Rev.* **1**, CD003869 (2018).
8. Patchell, R. A. et al. Postoperative radiotherapy in the treatment of single metastases to the brain: a randomized trial. *JAMA* **280**, 1485–1489 (1998).
9. Hong, A. M. et al. Adjuvant whole-brain radiation therapy compared with observation after local treatment of melanoma brain metastases: a multicenter, randomized phase III trial. *J. Clin. Oncol.* **37**, 3132–3141 (2019).

10. Brown, P. D. et al. Effect of radiosurgery alone vs radiosurgery with whole brain radiation therapy on cognitive function in patients with 1 to 3 brain metastases: a randomized clinical trial. *JAMA* **316**, 401–409 (2016).
11. Brown, P. D. et al. Postoperative stereotactic radiosurgery compared with whole brain radiotherapy for resected metastatic brain disease (NCCTG N107C/CEC·3): a multicentre, randomised, controlled, phase 3 trial. *Lancet Oncol.* **18**, 1049–1060 (2017).
12. Chang, E. L. et al. Neurocognition in patients with brain metastases treated with radiosurgery or radiosurgery plus whole-brain irradiation: a randomised controlled trial. *Lancet Oncol.* **10**, 1037–1044 (2009).
13. Aoyama, H. et al. Stereotactic radiosurgery plus whole-brain radiation therapy vs stereotactic radiosurgery alone for treatment of brain metastases: a randomized controlled trial. *JAMA* **295**, 2483–2491 (2006).
14. Nabors, L. B. et al. NCCN guidelines insights: central nervous system cancers, version 1.2017. *J. Natl Compr. Cancer Netw.* **15**, 1331–1345 (2017).
15. Soffietti, R. et al. Diagnosis and treatment of brain metastases from solid tumors: guidelines from the European Association of Neuro-Oncology (EANO). *Neuro. Oncol.* **19**, 162–174 (2017).
16. Suh, J. H. et al. Current approaches to the management of brain metastases. *Nat. Rev. Clin. Oncol.* **17**, 279–299 (2020).
17. Minniti, G. et al. Stereotactic radiosurgery for brain metastases: analysis of outcome and risk of brain radionecrosis. *Radiat. Oncol.* **6**, 48 (2011).
18. Donovan, E. K., Parpia, S. & Greenspoon, J. N. Incidence of radionecrosis in single-fraction radiosurgery compared with fractionated radiotherapy in the treatment of brain metastasis. *Curr. Oncol.* **26**, e328–e333 (2019).
19. Martin, A. M. et al. Immunotherapy and symptomatic radiation necrosis in patients with brain metastases treated with stereotactic radiation. *JAMA Oncol.* **4**, 1123–1124 (2018).
20. Smith, D. L., Debeb, B. G., Thames, H. D. & Woodward, W. A. Computational modeling of micrometastatic breast cancer radiation dose response. *Int. J. Radiat. Oncol. Biol. Phys.* **96**, 179–187 (2016).
21. Choi, S. H. et al. TopBP1 and Claspin contribute to the radioresistance of lung cancer brain metastases. *Mol. Cancer* **13**, 211 (2014).
22. Yang, H. et al. Radiosensitization of brain metastasis by targeting c-MET. *Lab. Invest.* **93**, 344–353 (2013).
23. Baschnagel, A. et al. Vorinostat enhances the radiosensitivity of a breast cancer brain metastatic cell line grown in vitro and as intracranial xenografts. *Mol. Cancer Ther.* **8**, 1589–1595 (2009).
24. Martínez-Aranda, A., Hernández, V., Picón, C., Modolell, I. & Sierra, A. Development of a preclinical therapeutic model of human brain metastasis with chemoradiotherapy. *Int. J. Mol. Sci.* **14**, 8306–8327 (2013).
25. Smart, D. et al. Analysis of radiation therapy in a model of triple-negative breast cancer brain metastasis. *Clin. Exp. Metastasis* **32**, 717–727 (2015).
26. Leder, K. et al. Mathematical modeling of PDGF-driven glioblastoma reveals optimized radiation dosing schedules. *Cell* **156**, 603–616 (2014).
27. Nguyen, D. X. et al. WNT/TCF signaling through LEF1 and HOXB9 mediates lung adenocarcinoma metastasis. *Cell* **138**, 51–62 (2009).
28. Johnstone, C. N. et al. Functional and molecular characterisation of EO771. LMB tumours, a new C57BL/6-mouse-derived model of spontaneously metastatic mammary cancer. *Dis. Model. Mech.* **8**, 237–251 (2015).
29. Valiente, M. et al. Serpins promote cancer cell survival and vascular co-option in brain metastasis. *Cell* **156**, 1002–1016 (2014).
30. Priego, N. et al. STAT3 labels a subpopulation of reactive astrocytes required for brain metastasis. *Nat. Med.* **24**, 1024–1035 (2018).
31. Er, E. E. et al. Pericyte-like spreading by disseminated cancer cells activates YAP and MRTF for metastatic colonization. *Nat. Cell Biol.* **20**, 966–978 (2018).
32. Celià-Terrassa, T. & Kang, Y. Distinctive properties of metastasis-initiating cells. *Genes Dev.* **30**, 892–908 (2016).
33. Batlle, E. & Clevers, H. Cancer stem cells revisited. *Nat. Med.* **23**, 1124–1134 (2017).
34. Oskarsson, T. et al. Breast cancer cells produce tenascin C as a metastatic niche component to colonize the lungs. *Nat. Med.* **17**, 867–874 (2011).
35. Wasilewski, D., Priego, N., Fustero-Torre, C. & Valiente, M. Reactive astrocytes in brain metastasis. *Front. Oncol.* **7**, 298 (2017).
36. Chen, Q. et al. Carcinoma-astrocyte gap junctions promote brain metastasis by cGAMP transfer. *Nature* **533**, 493–498 (2016).
37. Lin, Q. et al. Reactive astrocytes protect melanoma cells from chemotherapy by sequestering intracellular calcium through gap junction communication channels. *Neoplasia* **12**, 748–754 (2010).
38. Choy, C. et al. Cooperation of neurotrophin receptor TrkB and Her2 in breast cancer cells facilitates brain metastases. *Breast Cancer Res.* **19**, 51 (2017).
39. Schwartz, H. et al. Incipient melanoma brain metastases instigate astrogliosis and neuroinflammation. *Cancer Res.* **76**, 4359–4371 (2016).
40. Schildge, S., Bohrer, C., Beck, K. & Schachtrup, C. Isolation and culture of mouse cortical astrocytes. *J. Vis. Exp.* https://doi.org/10.3791/50079 (2013).
41. Hermani, A., De Servi, B., Medunjanin, S., Tessier, P. A. & Mayer, D. S100A8 and S100A9 activate MAP kinase and NF-kappaB signaling pathways and trigger translocation of RAGE in human prostate cancer cells. *Exp. Cell Res.* **312**, 184–197 (2006).
42. Shabani, F., Farasat, A., Mahdavi, M. & Gheibi, N. Calprotectin (S100A8/S100A9): a key protein between inflammation and cancer. *Inflamm. Res.* **67**, 801–812 (2018).
43. Markowitz, J. & Carson, W. E. Review of S100A9 biology and its role in cancer. *Biochim. Biophys. Acta* **1835**, 100–109 (2013).
44. Wang, R. et al. Inhibition of NF-κB improves sensitivity to irradiation and EGFR-TKIs and decreases irradiation-induced lung toxicity. *Int. J. Cancer* **144**, 200–209 (2019).
45. Yang, C. et al. A20/TNFAIP3 regulates the DNA damage response and mediates tumor cell resistance to DNA-damaging therapy. *Cancer Res.* **78**, 1069–1082 (2018).
46. Bhat, K. P. L. et al. Mesenchymal differentiation mediated by NF-κB promotes radiation resistance in glioblastoma. *Cancer Cell* **24**, 331–346 (2013).
47. Lim, S. Y., Yuzhalin, A. E., Gordon-Weeks, A. N. & Muschel, R. J. Tumor-infiltrating monocytes/macrophages promote tumor invasion and migration by upregulating S100A8 and S100A9 expression in cancer cells. *Oncogene* **35**, 5735–5745 (2016).
48. Hibino, T. et al. S100A9 is a novel ligand of EMMPRIN that promotes melanoma metastasis. *Cancer Res.* **73**, 172–183 (2013).
49. Eisenblaetter, M. et al. Visualization of tumor-immune interaction: target-specific imaging of S100A8/A9 reveals pre-metastatic niche establishment. *Theranostics* **7**, 2392–2401 (2017).
50. Hiratsuka, S., Watanabe, A., Aburatani, H. & Maru, Y. Tumour-mediated upregulation of chemoattractants and recruitment of myeloid cells predetermines lung metastasis. *Nat. Cell Biol.* **8**, 1369–1375 (2006).
51. Acharyya, S. et al. A CXCL1 paracrine network links cancer chemoresistance and metastasis. *Cell* **150**, 165–178 (2012).
52. Biswas, A. K. et al. Targeting S100A9-ALDH1A1-retinoic acid signaling to suppress brain relapse in EGFR-mutant lung cancer. *Cancer Discov.* https://doi.org/10.1158/2159-8290.CD-21-0910 (2022).
53. Zhu, L. et al. A drug-screening platform based on organotypic cultures identifies vulnerabilities to prevent local relapse and treat established brain metastasis. *EMBO Mol. Med.* https://doi.org/10.1101/2020.10.16.329243 (2022).
54. Garaulet, G. et al. IL10 released by a new inflammation-regulated lentiviral system efficiently attenuates zymosan-induced arthritis. *Mol. Ther.* **21**, 119–130 (2013).
55. Garaulet, G. et al. Intratumoral expression using a NFkB-based promoter enhances IL12 antitumor efficacy. *Cancer Gene Ther.* **26**, 216–233 (2019).
56. Malladi, S. et al. Metastatic latency and immune evasion through autocrine inhibition of WNT. *Cell* **165**, 45–60 (2016).
57. Slyper, M. et al. A single-cell and single-nucleus RNA-Seq toolbox for fresh and frozen human tumors. *Nat. Med.* **26**, 792–802 (2020).
58. Tang, L. et al. Role of metabolism in cancer cell radioresistance and radiosensitization methods. *J. Exp. Clin. Cancer Res.* **37**, 87 (2018).
59. Vareslija, D. et al. Transcriptome characterization of matched primary breast and brain metastatic tumors to detect novel actionable targets. *J. Natl Cancer Inst.* **111**, 388–398 (2019).
60. Cosgrove, N. et al. Mapping molecular subtype specific alterations in breast cancer brain metastases identifies clinically relevant vulnerabilities. *Nat. Commun.* **13**, 514 (2022).
61. Stupp, R. et al. Effects of radiotherapy with concomitant and adjuvant temozolomide versus radiotherapy alone on survival in glioblastoma in a randomised phase III study: 5-year analysis of the EORTC-NCIC trial. *Lancet Oncol.* **10**, 459–466 (2009).
62. Deane, R. et al. A multimodal RAGE-specific inhibitor reduces amyloid β-mediated brain disorder in a mouse model of Alzheimer disease. *J. Clin. Invest.* **122**, 1377–1392 (2012).
63. Moding, E. J., Kastan, M. B. & Kirsch, D. G. Strategies for optimizing the response of cancer and normal tissues to radiation. *Nat. Rev. Drug Discov.* **12**, 526–542 (2013).
64. Monje, M. L., Mizumatsu, S., Fike, J. R. & Palmer, T. D. Irradiation induces neural precursor-cell dysfunction. *Nat. Med.* **8**, 955–962 (2002).
65. Markarian, M. et al. Glia-selective deletion of complement C1q prevents radiation-induced cognitive deficits and neuroinflammation. *Cancer Res.* **81**, 1732–1744 (2021).
66. Bhat, K. et al. 1-[(4-Nitrophenyl)sulfonyl]-4-phenylpiperazine treatment after brain irradiation preserves cognitive function in mice. *Neuro. Oncol.* **22**, 1484–1494 (2020).
67. van der Meer, M., Rolls, A., Baumans, V., Olivier, B. & van Zutphen, L. F. Use of score sheets for welfare assessment of transgenic mice. *Lab Anim.* **35**, 379–389 (2001).
68. Crawley, J. N. *What's Wrong With My Mouse? Behavioral Phenotyping of Transgenic and Knockout Mice* (Wiley-Liss, 2007).
69. Hammelrath, L. et al. Morphological maturation of the mouse brain: an in vivo MRI and histology investigation. *Neuroimage* **125**, 144–152 (2016).
70. Boretius, S., Kasper, L., Tammer, R., Michaelis, T. & Frahm, J. MRI of cellular layers in mouse brain in vivo. *Neuroimage* **47**, 1252–1260 (2009).

71. Burstein, A. H. et al. Effect of TTP488 in patients with mild to moderate Alzheimer's disease. *BMC Neurol.* **14**, 12 (2014).
72. Burstein, A. H. et al. Development of azeliragon, an oral small molecule antagonist of the receptor for advanced glycation endproducts, for the potential slowing of loss of cognition in mild alzheimer's disease. *J. Prev. Alzheimers Dis.* **5**, 149–154 (2018).
73. Sabbagh, M. N. et al. PF-04494700, an oral inhibitor of receptor for advanced glycation end products (RAGE), in Alzheimer disease. *Alzheimer Dis. Assoc. Disord.* **25**, 206–212 (2011).
74. Ma, L., Carter, R. J., Morton, A. J. & Nicholson, L. F. B. RAGE is expressed in pyramidal cells of the hippocampus following moderate hypoxic-ischemic brain injury in rats. *Brain Res.* **966**, 167–174 (2003).
75. Sasaki, N. et al. Immunohistochemical distribution of the receptor for advanced glycation end products in neurons and astrocytes in Alzheimer's disease. *Brain Res.* **888**, 256–262 (2001).
76. Muhammad, S. et al. The HMGB1 receptor RAGE mediates ischemic brain damage. *J. Neurosci.* **28**, 12023–12031 (2008).
77. Kamide, T. et al. RAGE mediates vascular injury and inflammation after global cerebral ischemia. *Neurochem. Int.* **60**, 220–228 (2012).

[1]Brain Metastasis Group, CNIO, Madrid, Spain. [2]Bioinformatics Unit, CNIO, Madrid, Spain. [3]Histopathology Core Unit, CNIO, Madrid, Spain. [4]Department of Translational Neuroscience, Cajal Institute, CSIC, Madrid, Spain. [5]Neuro-Oncology Unit, Hospital Universitario 12 de Octubre, Madrid, Spain. [6]Neurosurgery Unit, Hospital Universitario 12 de Octubre, Madrid, Spain. [7]Department of Surgery, Universidad Complutense de Madrid, Madrid, Spain. [8]Neuropathology Unit, Hospital Universitario 12 de Octubre, Madrid, Spain. [9]Medical Oncology, Hospital Universitario 12 de Octubre, Madrid, Spain. [10]CNIO-H12O Clinical Cancer Research Unit, Fundación de Investigación Biomédica i+12 and CNIO, Madrid, Spain. [11]CIBERONC. [12]Department of Medicine, Universidad Complutense de Madrid, Madrid, Spain. [13]Radiation Oncology Department, Institut Claudius Regaud, IUCT-Oncopole, Toulouse, France. [14]Anatomopathology Department, CHU Toulouse, IUCT-Oncopole, Toulouse, France. [15]Endocrine Oncology Research Group, RCSI University of Medicine and Health Sciences, Dublin, Ireland. [16]Department of Neurosurgery, University Medical Center Hamburg-Eppendorf, Hamburg, Germany. [17]Department of Radiation Oncology, University Medical Center Hamburg-Eppendorf, Hamburg, Germany. [18]Department of Tumor Biology, University Medical Center Hamburg-Eppendorf, Hamburg, Germany. [19]Department of Neurosurgery, Hospital Universitario de La Princesa, Madrid, Spain. [20]Department of Pathology, Hospital Universitario La Paz, Madrid, Spain. [21]Cancer Prevention and Control Program, Fox Chase Cancer Center, Philadelphia, PA, USA. [22]Champalimaud Research, Champalimaud Centre for the Unknown, Lisbon, Portugal. [23]Instituto de Medicina Molecular João Lobo Antunes, Facultade de Medicina, Universidade de Lisboa, Lisboa, Portugal. [24]Department of Neurosurgery, Hospital de Santa Maria, Centro Hospitalar Universitário Lisboa Norte (CHULN), Lisboa, Portugal. [25]Faculty of Biology Medicine and Health, The University of Manchester, Manchester, UK. [26]The Christie NHS Foundation Trust, Manchester, UK. [27]Department of Neurology, University Hospital Zurich, Zurich, Switzerland. [28]Division of Neuro-Oncology, Department of Neuroscience Rita Levi Montalcini, University of Turin, Turin, Italy. [29]Department of Medical Sciences, University of Turin, Turin, Italy. [30]Department of Oncology, University of Turin, Turin, Italy. [31]Department of Medical Oncology, Catalan Institute of Oncology, Doctor Josep Trueta University Hospital, Girona, Spain. [32]Girona Biomedical Research Institute (IDIBGi), Salt, Spain. [33]Department of Medical Sciences, University of Girona, Girona, Spain. [34]IDISNA, Program in Solid Tumors, Center for Applied Medical Research (CIMA), University of Navarra, Pamplona, Spain. [35]Department of Oncology, University Clinic of Navarra, Madrid, Spain. [36]Department of Oncology, University Clinic of Navarra, Pamplona, Spain. [37]Department of Biochemistry, University Clinic of Navarra, Pamplona, Spain. [38]Department of Pathology, Sackler Faculty of Medicine, Tel Aviv University, Tel Aviv, Israel. [39]Present address: Departments of Medicine and Biomedical Sciences, Cedars-Sinai Cancer, Cedars-Sinai Medical Center, Los Angeles, CA, USA. [41]These authors contributed equally: Cátia Monteiro, Lauritz Miarka. *A list of authors and their affiliations appears at the end of the paper. ✉e-mail: mvaliente@cnio.es